Inorganic Chemistry

Article

pubs.acs.org/IC

Probing the Noninnocent π-Bonding Influence of *N*-Carboxyamidoquinolate Ligands on the Light Harvesting and Redox Properties of Ruthenium Polypyridyl Complexes

Ken T. Ngo,[†] Nicholas A. Lee,[†] Sashari D. Pinnace,[†] David J. Szalda,[§] Ralph T. Weber,[‡] and Jonathan Rochford*[,†]

[†]Department of Chemistry, University of Massachusetts Boston, 100 Morrissey Boulevard, Boston, Massachusetts 02125, United States

[‡]EPR Division, Bruker BioSpin Corporation, 44 Manning Road, Billerica, Massachusetts 01821, United States

[§]Chemistry Department, Baruch College, New York, New York 10010, United States

Supporting Information

ABSTRACT: Electronic and photophysical characterization is presented for a series of bis-heteroleptic $[Ru(bpy)_2(R\text{-}CAQN)]^+$ complexes where CAQN is a bidentate *N*-(carboxyaryl)-amidoquinolate ligand and the aryl substituent R = *p*-tolyl, *p*-fluorobenzene, *p*-trifluoromethylbenzene, 3,5-bis-(trifluoromethyl)benzene, or 4-methoxy-2,3,5,6-tetrafluorobenzene. Characterized by a strong noninnocent Ru(dπ)−CAQN-(π) bonding interaction, density functional theory (DFT) analysis is used to estimate the contribution of both atomic Ru(dπ) and ligand CAQN(π) manifolds to the frontier molecular orbitals of these complexes. UV−vis absorption and emission studies are presented where the noninnocent Ru(dπ)−CAQN(π) bonding scheme plays a major role in defining complex electronic and photophysical properties. Oxidation potentials are tuned over a range of 0.92 V with respect to the $[Ru(bpy)_3]^{2+}$ reference system, hereafter referred to as $\mathbf{1}^{2+}$, by varying the degree of R-CAQN fluorination while maintaining consistently strong and panchromatic visible absorption properties. Electron paramagnetic resonance (EPR) spectroscopy is employed to experimentally map delocalization of the unpaired electron/electron−hole within the delocalized Ru(dπ)−CAQN(π) singly occupied valence molecular orbital of the one-electron oxidized complexes. EPR data is complemented experimentally by UV−vis−NIR spectroelectrochemistry, and computationally by molecular orbital Mulliken contributions and spin-density analysis. It is ultimately demonstrated that the CAQN ligand framework provides a simple yet broad synthetic platform in the design of redox-active transition metal chromophores with a range of electronic and spectroscopic characteristics hinting at the diversity and potential of these complexes toward photochemical and catalytic applications.

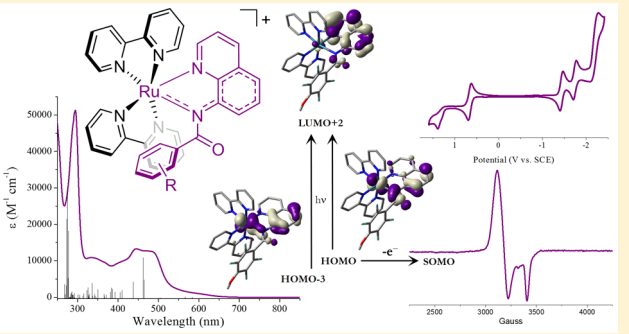

INTRODUCTION

Metal complexes incorporating noninnocent ligands (NILs) are growing increasingly important as a strategy to allow for unique opportunities in engineering molecular redox properties.[1−3] Often used interchangeably with the term redox-active, noninnocent ligands derive their label from the fact that they participate in extensive π-overlap with metal based atomic orbitals resulting in highly delocalized molecular orbitals.[4,5] Thus, one may consider NILs to be a subset of the redox-active ligand family, having significant consequences on the electronic structure of the complex as opposed to just displaying redox activity.[6] The purpose of this study is to investigate the noninnocent nature of the *N*-(carboxyaryl)amidoquinolate (CAQN) ligand system at the d^6 Ru(II) center. Ru(II) polypyridyl complexes are well-established at providing an ideal platform for metal d(π)−ligand(π) covalent mixing and have a broad interest for photophysical and catalytic applications.[7−12] Motivation for studying the CAQN ligand stems from an interest in evaluating the transition metal bonding properties of asymmetric NIL frameworks, building upon the more common cyclometalated phenylpyridine (ppy), oxyquinolate (OQN), and β-ketoiminate systems.[8,13,14] To the best of our knowledge there only exists a single prior report of a ruthenium CAQN complex where Ru(η^6-*p*-cymene) (Ph-CAQN)Cl was utilized as a catalyst for the synthesis of isoquinolones via oxidative annulation of *N*-quinolin-8-yl-benzamides with alkynes.[15] Furthermore, only a handful of structural and catalysis based reports exist for CAQN type ligands with alternative (Ti, Fe, Co, Ni, Cu, Pd, Ir) transition metal centers.[15−23] A family of bis-heteroleptic complexes containing a series of CAQN ligands at the ruthenium(II)

Received: December 9, 2015

 © XXXX American Chemical Society

DOI: 10.1021/acs.inorgchem.5b02834
Inorg. Chem. XXXX, XXX, XXX−XXX

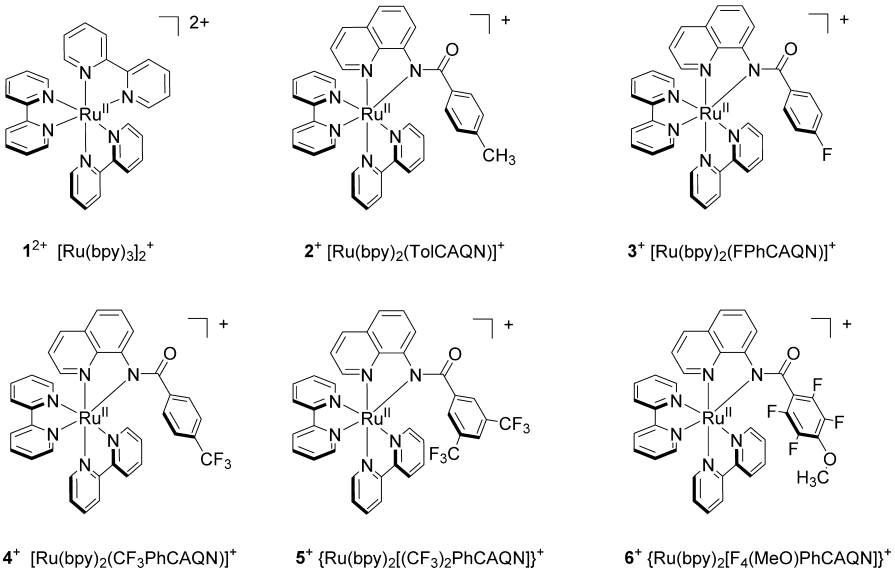

Figure 1. Structures of $[Ru(bpy)_2(R\text{-}CAQN)]^+$ complexes $\mathbf{2}^+$–$\mathbf{6}^+$ investigated here alongside the $\mathbf{1}^{2+}$ reference compound.

Scheme 1. (a) Synthetic Procedure Employed in the Synthesis of the *N*-(Carboxyaryl)-8-aminoquinoline (R-CAQN·H) Ligands and (b) Synthesis of the $[Ru(bpy)_2(R\text{-}CAQN)]^+$ Complexes

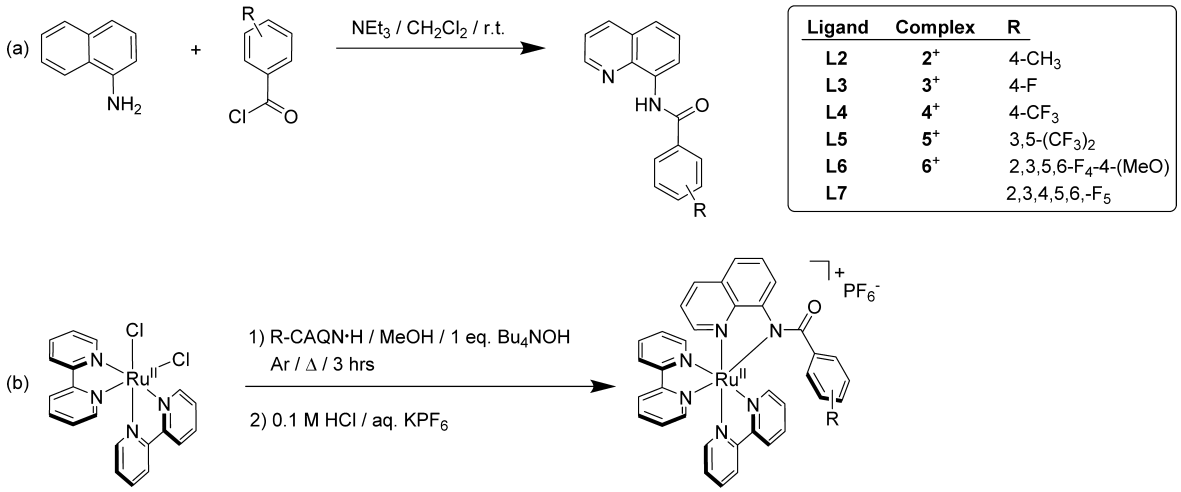

Ligand	Complex	R
L2	$\mathbf{2}^+$	4-CH_3
L3	$\mathbf{3}^+$	4-F
L4	$\mathbf{4}^+$	4-CF_3
L5	$\mathbf{5}^+$	3,5-$(CF_3)_2$
L6	$\mathbf{6}^+$	2,3,5,6-F_4-4-(MeO)
L7		2,3,4,5,6,-F_5

bis(2,2′-bipyridyl) core are presented here where varying degrees of fluorination are introduced on the carboxy aryl ring system in order to provide a means of tuning complex oxidation potentials while maintaining favorable photophysical properties (Figure 1). An in-depth spectroscopic and electrochemical analysis is presented, supported by computational studies, to give a detailed picture of complex photophysical and electronic properties.

RESULTS AND DISCUSSION

Synthesis and Structural Characterization. All amido ligand precursors were prepared by a simple one-pot condensation reaction between 8-aminoquinoline and the appropriate benzoyl chloride similar to a reported literature procedure (Scheme 1).[24] The deprotonated amido CAQN ligands are easily bound to the ruthenium(II) bis(2,2-bipydidyl) core in methanol solution with a stoichiometric quantity of base such as tetrabutyl ammonium hydroxide. $[Ru(bpy)_2(R\text{-}CAQN)](PF_6)$ salts were isolated via aqueous KPF_6 mediated metathesis followed by acetone/diethyl ether recrystallization resulting in analytically pure dark reddish-brown solids. Curiously, efforts to synthesize the perfluorinated $[Ru(bpy)_2(F_5Ph\text{-}CAQN)](PF_6)$ complex from ligand **L7** consistently resulted in quantitative formation of a complex whose molecular ion (m/z = 763.1) was 12 mass units higher than anticipated. A combination of ^1H and ^{19}F NMR studies confirmed the *p*-fluorine atom was replaced by a methoxy group, presumably from the methanol solvent, yielding complex $\mathbf{6}^+$. Although unexpected, etherification has been recently reported at the *m*-trifluoromethylphenyl ring of a CAQN ligand catalyzed by Cu(II).[25] Direct synthesis of $\mathbf{6}^+$ confirmed the complex regiochemistry following synthesis of the *N*-(4-methoxy-2,3,5,6-tetrafluorophenyl)-8-carboxyaminoquinoline ligand precursor **L6**. Attempts to isolate the perfluorinated ruthenium complex by changing a variety of reaction conditions (low temperature, aprotic solvents etc.) were in vain.

Single crystals of the tolyl-CAQN complex $\mathbf{2}(PF_6)\cdot 0.125H_2O$ suitable for X-ray diffraction were isolated by slow evaporation of methanol from an aqueous methanol solution. The complex crystallizes as a racemic mixture of Δ and Λ enantiomers with

DOI: 10.1021/acs.inorgchem.5b02834
Inorg. Chem. XXXX, XXX, XXX–XXX

one molecule of water of crystallization in the unit cell. The two 2^+ cations in the asymmetric unit are approximately related by a noncrystallographic inversion center with the quinoline rings of each cation slightly overlapped with a dihedral angle of 3.76(12)° and shortest C···C contacts of ∼3.4 Å. An ORTEP drawing of one of the cations of $2(PF_6)\cdot 0.125H_2O$ is presented in Figure 2. Most notable for both cations of the unit cell is π-

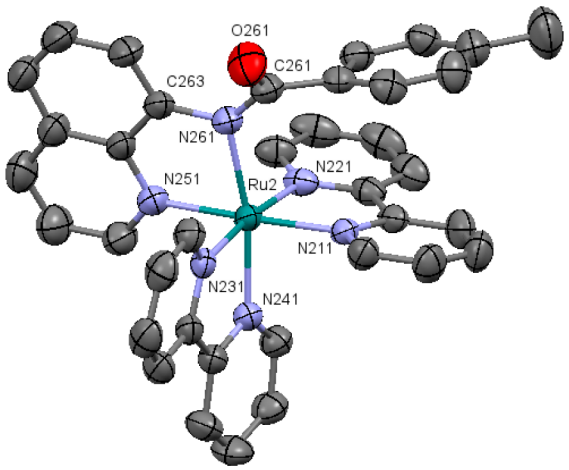

Figure 2. Ortep diagram of $2(PF_6)\cdot 0.125H_2O$ illustrating π-stacking of the tolyl-CAQN aryl substituent with an adjacent bpy ligand. Hydrogen atoms, the PF_6^- anion, and water of solvation have been removed for clarity.

stacking of the *N*-carboxytolyl substituent of the CAQN ligand with the adjacent bpy ligand at the ruthenium center; plane-to-plane ring distance = 3.538 Å, and a plane-to-plane dihedral angle = 11.4(2)° and 12.6(2)° for either enantiomer. Similar π-stacking has been previously observed for $[Ru(bpy)_2(2\text{-arylphenanthroline})]^+$ complexes and has been shown to improve the stability of excited state ligand field states.[26] Figure 2 shows clearly that the tolyl group is rotated with respect to the amide bond (dihedral angle = 46.58°) to facilitate the observed π-stacking, however, not to the extent where the electronic influence of the aryl ring is silenced (vide infra). It should be noted however that observation of such π-stacking in the solid state does not rule out rotation of the carboxy−aryl bond at room temperature in solution phase, which may even promote electronic communication with the quinoline ring.

Computational Analysis. Density functional theory analysis was carried out on complexes 1^{2+}−6^+ to inform qualitatively and quantitatively on the relative extent of ruthenium(dπ)−CAQN(π) mixing in the frontier orbitals of each complex. Qualitatively, the bonding versus antibonding character and delocalization of ruthenium(dπ)−CAQN(π) overlap can be ascertained by visual inspection of the resulting molecular orbital surfaces. From a quantitative perspective, the influence of ruthenium(dπ)−CAQN(π) mixing on relative frontier orbital energies is determined by investigation of Mulliken molecular orbital contributions and the contribution of these frontier orbitals to the visible electronic transitions of each complex analyzed by time-dependent density functional theory (TDDFT). It should be appreciated that the extent of metal−ligand mixing inferred by Mulliken molecular orbital contributions can vary depending upon the choice of basis set.[27] As such, any quantitative DFT MO contribution analysis here presented is not deemed absolute but merely used to aid interpretation of spectroscopic and electrochemical behavior of these complexes. For brevity, a detailed comparison of 1^{2+} relative to just the $[Ru(bpy)_2(tolyl\text{-}CAQN)]^+$ complex 2^+ is presented in Figure 3. The bonding scheme for 1^{2+} is described according to *pseudo-*O_h symmetry in Figure 3a and consists primarily of M−L σ-bonding with negligible π-bonding between the metal center and the ligand set.[28] The nonbonding filled HOMO and degenerate (HOMO − 1, HOMO − 2) d atomic orbitals, and virtual LUMO and degenerate (LUMO + 1, LUMO + 2) unoccupied bpy(π*) levels, are distinctive for this classical coordination complex and are responsible for the typical singlet metal-to-ligand charge-transfer (^{1}MLCT) electronic transitions observed for so many ruthenium polypyridyl systems.[29,30] In contrast, introduction of the π-donating tolyl-CAQN anion at the ruthenium center significantly perturbs the classical M−L σ-bonding scenario. First, a reduction in symmetry from *pseudo-*O_h to *pseudo-*C_s breaks down any energy level degeneracy.[31] Electron donation from both the tolyl-CAQN anion and a filled Ru(d) atomic orbital gives rise to covalent Ru(dπ)−CAQN(π) molecular orbital overlap. The resultant bonding (HOMO − 3) and antibonding (HOMO) levels are distinct from 1^{2+} in that they each contain a significant mixture of metal and ligand contributions. Furthermore, due to destabilization of the HOMO level, a narrowing of the HOMO−LUMO band gap is observed where the LUMO is still predominantly bpy(π*) in character. As a result of this Ru(dπ)−CAQN(π) mixing the HOMO → LUMO charge-transfer excitation is now more accurately described as a singlet (metal−ligand)-to-ligand charge-transfer (^{1}MLLCT) transition and is accessible with lower energy radiation.

The molecular orbital surfaces presented in Figure 3b for the HOMO and HOMO − 3 levels of 2^+ show clear evidence of the π-antibonding and π-bonding Ru(dπ)−CAQN(π) character, respectively, at the Ru−N_{amido} interface. This Ru(dπ)−CAQN(π) interaction is noteworthy as the character of these frontier orbitals contributes significantly to the enhanced light harvesting of 2^+ as determined by TDDFT analysis. The TDDFT absorption spectrum of 1^{2+} is characterized by a single ^{1}MLCT absorption band derived from an isoenergetic mixture of HOMO − 1/HOMO − 2 → LUMO/LUMO + 1/LUMO + 2 ^{1}MLCT electronic transitions (Table SI-1). Complex 2^+ on the other hand displays a much broader TDDFT absorption profile stretching from the UV across the entire visible range due to a diverse set of underlying electronic transitions. The dominant electronic transitions observed for 2^+ are a mixture of ^{1}MLCT and ^{1}MLLCT character. The calculated TDDFT absorption spectrum shows excellent qualitative agreement with experiment as illustrated in Figure 3c. A more detailed discussion of spectral assignments is discussed below for all complexes. Table 1 summarizes the percentage Mulliken contribution of Ru(d) and ligand(π) orbitals to the relevant HOMO and HOMO − 3 energy levels for complexes 2^+−6^+ to illustrate the noninnocent Ru(dπ)−CAQN(π) bonding interaction across the series. A summary of frontier orbital surfaces and corresponding energies for complexes 1^{2+}−6^+ is presented in Figure 4.

UV−Vis Electronic Absorption Spectra and TDDFT. The photophysical properties of 1^{2+} have been studied on many occasions and are well-established.[30,32,33] As briefly discussed above, 1^{2+} displays a characteristic absorption maximum at 450 nm (ε = 14 600 M^{-1} cm^{-1}) due to a series of unresolved ^{1}MLCT electronic transitions (Figure 3a, Table SI-1). Each of

DOI: 10.1021/acs.inorgchem.5b02834
Inorg. Chem. XXXX, XXX, XXX−XXX

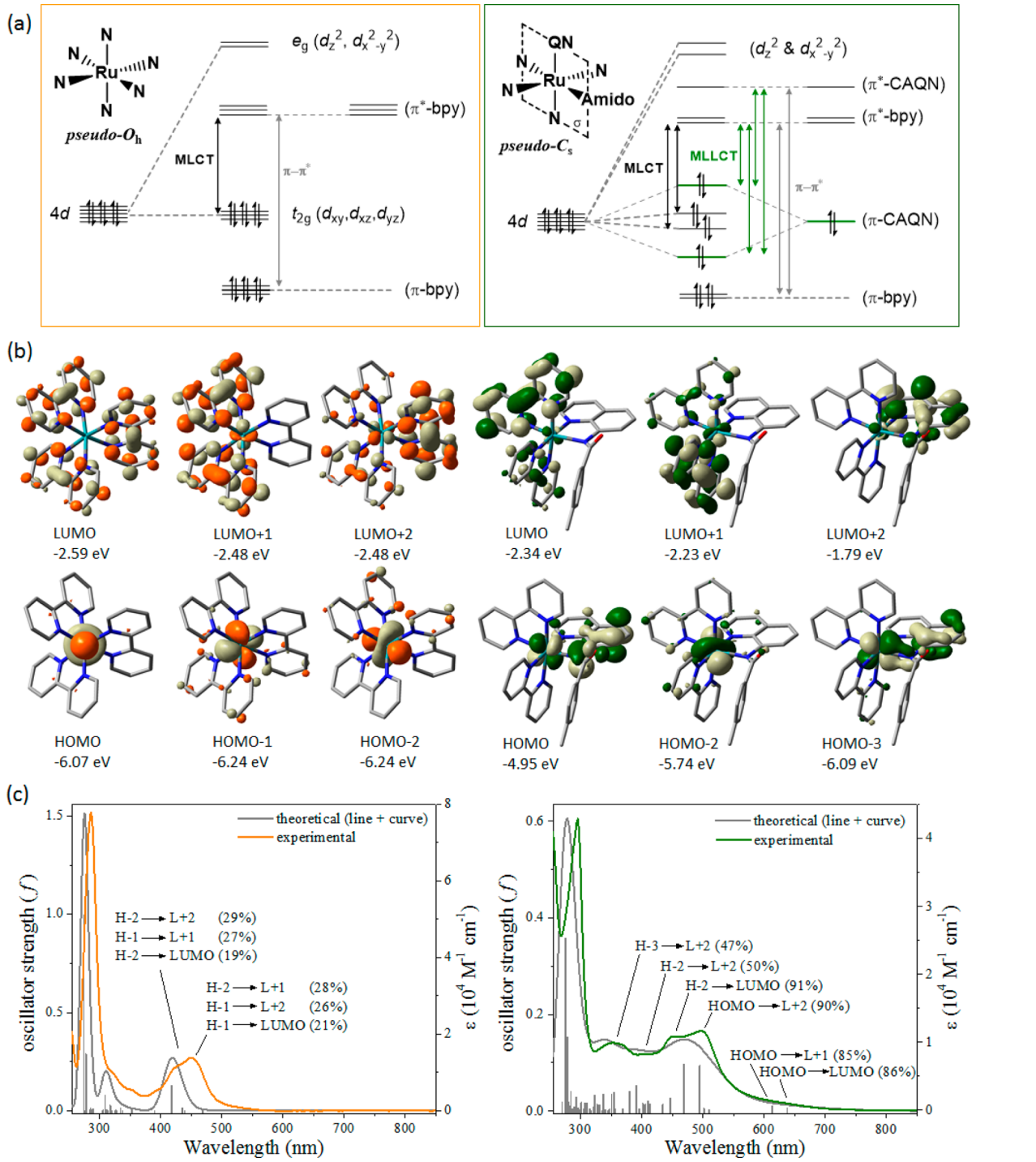

Figure 3. (a) Molecular orbital correlation diagrams and (b) select frontier molecular orbital surfaces (isofactor = 0.04) for $\mathbf{1}^{2+}$ and $\mathbf{2}^{+}$. (c) An overlay of experimental and computational (TDDFT) UV−vis spectra is also included for both complexes with quantitative TDDFT assignments to illustrate the influence of the π-donating noninnocent CAQN ligand on the observed electronic transitions.

the ruthenium CAQN complexes $\mathbf{2}^{+}$−$\mathbf{6}^{+}$ display very similar spectra where replacement of one of the bpy ligands on $\mathbf{1}^{2+}$ with a noninnocent CAQN ligand gives rise to enhanced light harvesting due to a broader and red-shifted absorption profile. The degree of fluorination at the *N*-carboxyaryl ring substituent has limited influence on the light harvesting properties across the series with just a slight blue shift of the lowest energy absorption maximum observed with increased fluorination/decreased CAQN donor strength (Figure 5 and Table 2).

The broad absorption profile observed for $\mathbf{2}^{+}$−$\mathbf{6}^{+}$ is due to a range of both ^{1}MLCT and ^{1}MLLCT electronic transitions stretching across the UV−vis spectrum consistent with their reduced *pseudo-*C_s symmetry relative to $\mathbf{1}^{2+}$. The high energy absorption bands ranging from 334 to 353 nm and the low energy absorption maxima ranging from 471 to 497 nm across the series are highly characteristic of the Ru(dπ)−CAQN(π) bonding in these complexes. According to TDDFT analysis, both of these absorption bands are ^{1}MLLCT [Ru(dπ)-CAQN(π)] → CAQN(π^*) in character originating from the

DOI: 10.1021/acs.inorgchem.5b02834
Inorg. Chem. XXXX, XXX, XXX−XXX

Table 1. Mulliken Percentage Population Analysis of the HOMO and HOMO − 3 Levels for Complexes 2^+−6^+ Determined by DFT Analysis[a]

		Ru d(π)	R-CAQN(π)	bpy (total)	energy (eV)
1^{2+}	HOMO	88		12	−6.070
2^+	HOMO	28	68	4	−4.948
	HOMO − 3	56	35	9	−6.089
3^+	HOMO	28	68	4	−4.986
	HOMO − 3	56	35	9	−6.111
4^+	HOMO	29	67	4	−5.012
	HOMO − 3	55	36	9	−6.132
5^+	HOMO	31	65	4	−5.114
	HOMO − 3	53	38	9	−6.182
6^+	HOMO	36	59	5	−5.221
	HOMO − 3	49	43	8	−6.240

[a]Group contributions to the HOMO of 1^{2+} are included for comparison.

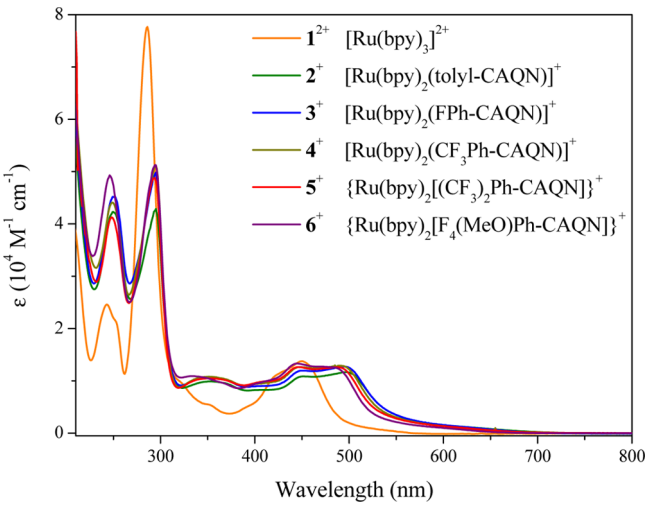

Figure 5. Overlay of UV−vis absorption spectra for [Ru(bpy)$_2$(R-CAQN)]$^+$ complexes recorded in acetonitrile with reference to 1^{2+}.

bonding (HOMO − 3) and antibonding (HOMO) Ru(dπ)−CAQN(π) orbitals, respectively, and terminating at the vacant CAQN(π^*) antibonding orbital (LUMO + 2). Thus, a major portion of the UV−vis absorption spectra for complexes 2^+−6^+ is derived entirely from the noninnocent Ru(dπ)−CAQN(π) bonding interaction. Of course traditional ^{1}MLCT electronic transitions of Ru(d) → bpy(π^*) and Ru(d) → CAQN(π^*) character are also observed via TDDFT analysis for complexes 2^+−6^+ giving rise to intermediate visible absorption bands, which are observed experimentally in the range 405−452 nm. The lowest energy absorption band tails out to ∼700 nm for all Ru-CAQN complex experimental spectra. This low energy absorption is attributed to weak oscillator strength HOMO → LUMO and HOMO → LUMO + 1 electronic transitions which are characterized as [Ru(dπ)-CAQN(π)] → bpy(π^*) charge-transfer transitions by TDDFT. A detailed database of TDDFT data for all complexes is provided in the Supporting Information.

Corrected low temperature ^{3}MLCT phosphorescence emission spectra of all dyes were recorded in a 77 K frozen ethanol/methanol (4:1) glass and are presented in Figure 6. As anticipated, due to CAQN destabilization of the HOMO level, a narrower $S_0 \leftarrow T_1$ energy gap (E_0) is observed ranging from 15 800 to 16 000 cm^{-1} relative to 17 900 cm^{-1} observed for 1^{2+}. Apart from complex 5^+, emission maxima shift to lower energy with increasing donor strength (decreased fluorination) of the CAQN ligand concomitant with an increased broadening and full width half maxima ($\Delta\nu_{1/2}$ ranges from 2200 to 2600 cm^{-1}) due to reduced vibrational spacing, e.g., $\hbar_{\omega M} \sim 685$ cm^{-1} for 6^+. Complex 5^+ shows the lowest energy and broadest emission

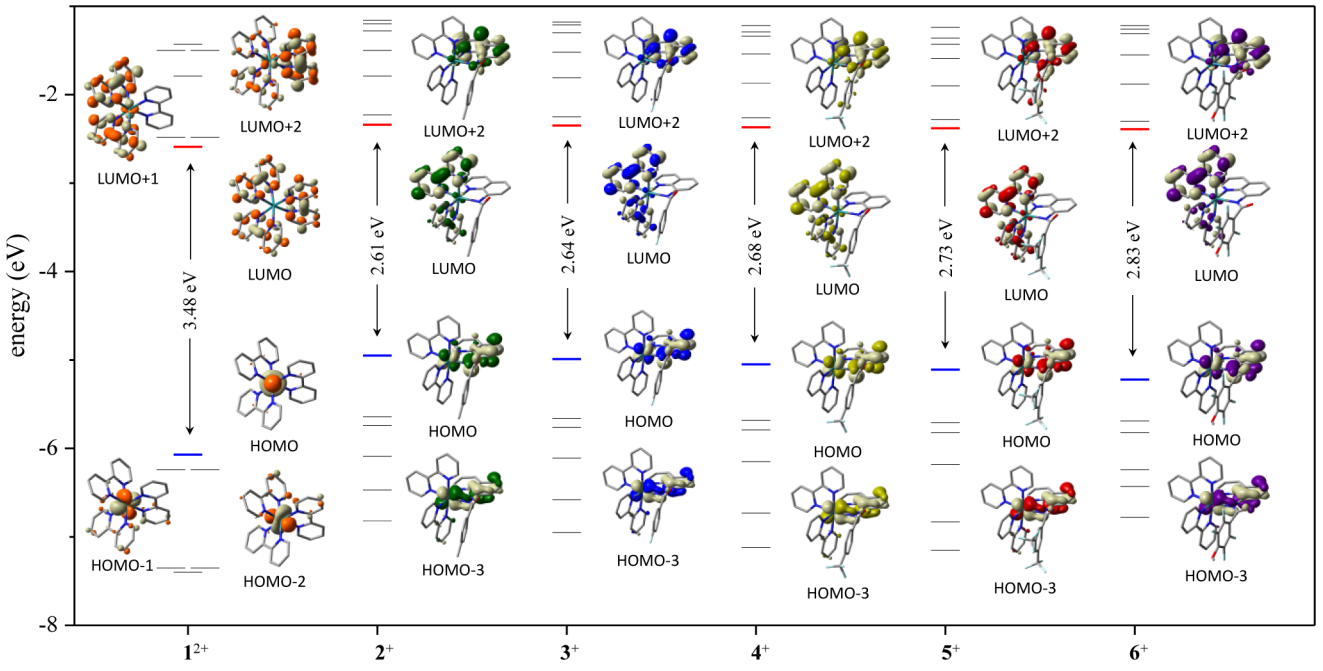

Figure 4. Plot of frontier molecular orbital energy levels (eV) for complexes 1^{2+}−6^+ as calculated by DFT/B3LYP/6-31g(d,p) (C,H,N,O,F) and LANL08 (Ru) in an acetonitrile polarizable continuum model. Electron occupancy is removed for clarity, and HOMO−LUMO levels are highlighted in blue and red, respectively. Select frontier molecular orbital surfaces (isofactor = 0.04) are included for comparison.

DOI: 10.1021/acs.inorgchem.5b02834
Inorg. Chem. XXXX, XXX, XXX−XXX

Table 2. UV−Vis Electronic Absorption and Phosphorescence Emission Data

	abs λ_{max} [a] (nm) ($\varepsilon \times 10^4$ M^{-1} cm^{-1})	em λ_{max} [b] (nm)
1^{2+}	243 (2.49), 286 (7.79), 430 (sh), 450 (1.46)	581, 630, 680 (sh)
2^{+}	250 (4.23), 295 (4.29,) 352 (0.99), 405 (sh, 0.82), 452 (1.09), 497 (1.17)	683, 739 (sh)
3^{+}	251 (4.53), 295 (4.98), 352 (1.06), 412 (sh, 0.91), 451 (1.20), 495 (1.27)	681, 737 (sh)
4^{+}	249 (4.41), 295 (5.12), 351 (1.08), 405 (sh, 0.95), 448 (1.27), 491 (1.29)	673, 728 (sh)
5^{+}	248 (4.13), 294 (4.87), 353 (1.05), 412 (sh, 0.99), 446 (1.26), 485 (1.26)	697, 758 (sh)
6^{+}	246 (4.93), 294 (5.13), 334 (1.09), 445 (1.33), 471 (1.27)	662, 707 (sh)

[a]Recorded at room temperature in acetonitrile. [b]recorded at 77 K in an ethanol:methanol (4:1) frozen glass.

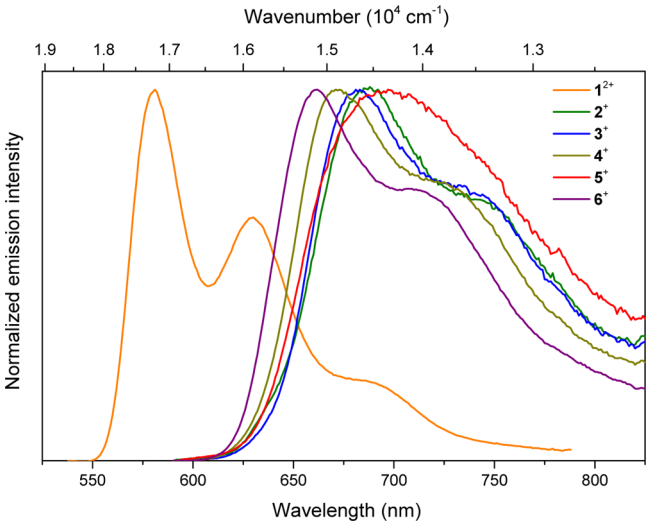

Figure 6. Overlay of corrected emission spectra recorded in a frozen EtOH/MeOH (4:1) glass at 77 K.

band with the least vibrational structure which is inconsistent with the remainder of the series. This is likely due to both trifluoromethyl substituents of the 3,5-bis(trifluoromethyl)-benzene-CAQN ligand having limited electron withdrawing influence at the meta positions of the aryl ring. All dyes display a much weaker photoluminescence relative to 1^{2+} consistent with the energy-gap law [$k_{nr} \propto \exp(-E_0)$] where the rate constant for nonradiative decay (k_{nr}) increases exponentially with a decreasing $S_0 \leftarrow T_1$ energy, thus precluding accurate determination of phosphorescence quantum yields.[34] In fact, all Ru-CAQN complexes 2^{+}−6^{+} are nonemissive at room temperature. This behavior is consistent with increased ^{3}MLLCT vibrational coupling due to significant Ru(dπ)−CAQN(π) mixing at the HOMO level (Table 1) and is reminiscent of the isoelectronic $[Ru(bpy)_2(ppy)]^+$ cyclometalated class of complexes.[35] While short excited state lifetimes and nonemissive behavior at room temperature may suggest poor applicability as a photosensitizer, there is precedent for related ruthenium complexes performing well in dye sensitized solar cells due to kinetically competitive reduction of the short-lived excited state by excess iodide ions in the redox mediator electrolyte.[36]

Electrochemistry. The electrochemical properties of all dyes were investigated by cyclic voltammetry. Consistent with destabilization of the HOMO level as predicted by DFT, as well as their red-shifted electronic spectra, all Ru-CAQN complexes show a strong cathodic shift of their first oxidation potential relative to 1^{2+}. The metal based Ru(III/II) couple of $1^{3+/2+}$ occurs at +1.29 V versus SCE. Replacing one of the bpy ligands with the strongest electron donating ligand tolyl-CAQN gives rise to a reversible first oxidation of $2^{2+/+}$ at +0.37 V versus SCE representing a potential shift of ΔE = −0.92 V. The least electron donating F_4(MeO)Ph-CAQN complex 6^{+} displays a reversible oxidation at +0.66 V versus SCE representing a potential shift of ΔE = −0.63 V relative to the $1^{3+/2+}$ couple. While a cathodic shift of oxidation potentials relative to 1^{2+} is primarily attributed to the π-donating influence of the R-CAQN ligands, one cannot rule out an additional Coulombic contribution due to the reduced charge of complexes 2^{+}−6^{+}. Unambiguous, however, is the 310 mV range of oxidation potentials observed for the $[Ru(bpy)_2(R\text{-}CAQN)]^{2+/+}$ redox couple induced by the degree of fluorination at the *N*-carboxyaryl substituent. Cyclic voltammograms of 1^{2+}, 2^{+}, and 6^{+} are presented in Figure 7 for comparison. Remaining Ru−CAQN complexes also display highly reversible first oxidations across a range of ∼0.92 V relative to 1^{+} and 2^{+} (Table 3).

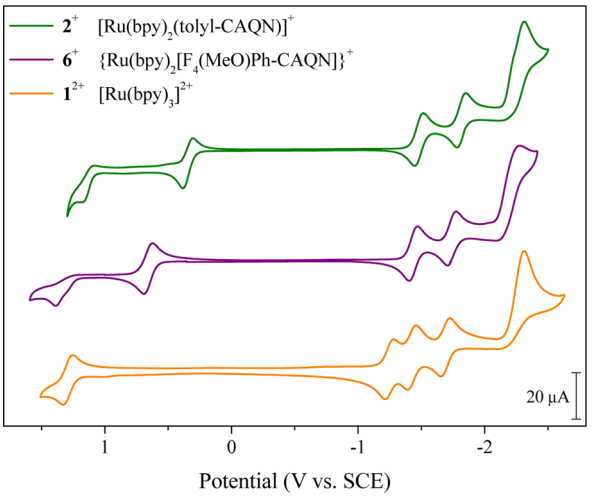

Figure 7. Cyclic voltammograms of 1^{2+}, 2^{+}, and 6^{+} recorded at room temperature in acetonitrile (0.1 M Bu_4NPF_6) at a glassy carbon working electrode with scan rate of 50 mV s^{-1}.

Unlike the $1^{3+/2+}$ redox couple that according to X-ray crystallography, DFT, and EPR analysis is predominantly metal based,[9,37] oxidation of Ru-CAQN complexes can potentially be described by two canonical resonance structures with Ru(III) or CAQN$^{\bullet}$ radical character. This is implied by the hybrid character of the HOMO level and is a result of the noninnocent

Table 3. Electrochemical Data for Complexes 1^{2+}−6^{+} Recorded in Acetonitrile (0.1 M Bu_4NPF_6) at a Glassy Carbon Working Electrode with a Scan Rate of 50 mV s^{-1}

	E (V vs SCE)					
1^{2+}		1.29	−1.33	−1.52	−1.76	−2.31[a]
2^{+}	1.21[a]	0.37	−1.46	−1.79	−2.29[a]	
3^{+}	1.23[a]	0.39	−1.46	−1.76	−2.29[a]	
4^{+}	1.26[a]	0.47	−1.45	−1.76	−2.23[a]	
5^{+}	1.23[a]	0.46	−1.51	−1.79	−2.31[a]	
6^{+}	1.39[a]	0.66	−1.44	−1.74	−2.28[a]	

[a]Irreversible.

DOI: 10.1021/acs.inorgchem.5b02834
Inorg. Chem. XXXX, XXX, XXX−XXX

Scheme 2. Structural Comparison of the $[Ru(bpy)_3]^{3+/2+}$ and $[Ru(bpy)_2(R\text{-}CAQN)]^{2+/+}$ Redox Couples Demonstrating Noninnocence of the CAQN Ligand via Resonance between a Ru(III) Center and a $CAQN^{\bullet}$ Radical

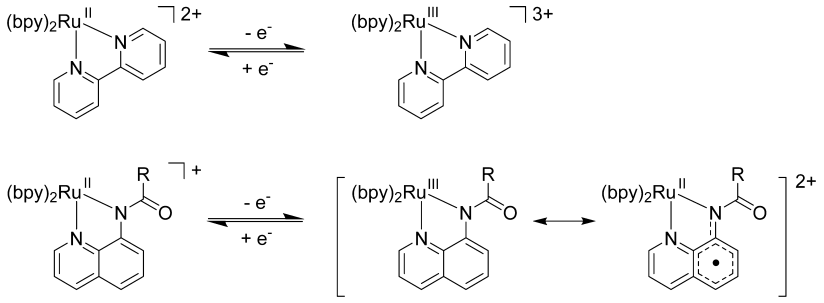

Ru(dπ)−CAQN(π) bonding interaction (Scheme 2). The hybrid nature of the HOMO is further corroborated by spectroelectrochemical UV−vis−NIR and EPR studies discussed below.

In contrast to $\mathbf{1}^{2+}$, all Ru-CAQN complexes also show an easily accessible irreversible second oxidation event occurring in the range from +1.21 V ($\mathbf{2}^{3+/2+}$) to +1.39 V ($\mathbf{6}^{3+/2+}$) versus SCE. This oxidation event most likely involves formation of the $Ru^{(IV)}$-$CAQN^{\bullet}$ species. Scanning in the negative direction, $\mathbf{1}^{2+}$ displays three sequential and reversible one-electron reduction events which are well-established as being bpy(π*)$^{0/\bullet-}$ based.[30] In fact, upon one-electron reduction of $\mathbf{1}^{2+}$ to $\mathbf{1}^{+}$, it can be considered formally isoelectronic to complexes $\mathbf{2}^{+}$−$\mathbf{6}^{+}$. Indeed all Ru-CAQN complexes display two reversible bpy(π*)$^{0/\bullet-}$ based reductions only slightly shifted relative to the second and third reductions of $\mathbf{1}^{2+}$. A third irreversible reduction event is also observed for all Ru-CAQN complexes. Whether this reduction event occurs on the CAQN or bpy ligands is unclear, however it is similar to a fourth irreversible reduction observed for $\mathbf{1}^{2+}$ at −2.31 V versus SCE.

Spectroelectrochemistry: Electron Paramagnetic Resonance. The combination of controlled potential electrolysis with EPR spectroscopy is a very powerful tool to probe the frontier orbital character of transition metal complexes.[38] EPR spectroscopy of paramagnetic transition metal complexes is capable of quantifying spin-density at the metal center via axial or rhombic *g*-anisotropy or by deviation of the isotropic *g*-factor ⟨*g*⟩ from that of the free electron *g*-factor (g_e = 2.0023).[39] The in situ generated one-electron oxidized $[Ru(bpy)_2(R\text{-}CAQN)]^{2+}$ complexes are hypothesized to have a singly occupied valence molecular orbital where the electron−hole is delocalized across the Ru(dπ)−CAQN(π) manifold due to the noninnocent nature of this system (Scheme 2). The one-electron oxidized species are EPR silent at room temperature due to a large Ru spin−orbital coupling constant ($\xi \sim 1000$ cm^{-1}) giving rise to fast relaxation times.[40] As such, controlled potential electrolysis was first completed at room temperature, and electrolyte solutions were subsequently transferred to an EPR tube under an inert argon atmosphere prior to freezing in liquid nitrogen. When recorded in a frozen glass, at first glance all $[Ru(bpy)(R\text{-}CAQN)]^{2+}$ EPR spectra appear to display axial *g*-anisotropy ($g_x = g_y \neq g_z$); however, the spectra fit best to a rhombic anisotropy ($g_x \neq g_y \neq g_z$). The Ru(III) centered radical in $\mathbf{1}^{3+}$ displays axial *g*-anisotropy and deviates most from the free electron *g*-factor (g_e = 2.0023) consistent with a maximum influence of Ru spin−orbital coupling. Increasing ligand contribution from the Ru(II)-$CAQN^{\bullet}$ resonance form (Scheme 2) decreases the Ru(III) contribution thus narrowing the *g*-factor splitting. This trend is best identified following the isotropic *g*-factor ⟨*g*⟩ summarized in Table 4. A maximum isotropic *g*-factor is observed at ⟨*g*⟩ = 2.140 for $\mathbf{1}^{3+}$ which decreases with increasing Ru(II)-$CAQN^{\bullet}$ contribution to a minimum value of ⟨*g*⟩ = 2.048 for $\mathbf{2}^{2+}$. An example of the EPR spectrum observed for $\mathbf{2}^{2+}$ is presented in Figure 8.

Table 4. EPR Data of Complexes $\mathbf{1}^{3+}$−$\mathbf{6}^{2+}$[a]

	g_x	g_y	g_z	Δg ($g_x - g_z$)	⟨*g*⟩
$\mathbf{1}^{3+}$[41]	2.640	2.640	1.140	1.500	2.140
$\mathbf{2}^{2+}$	2.118	2.067	1.959	0.159	2.048
$\mathbf{3}^{2+}$	2.119	2.068	1.958	0.161	2.048
$\mathbf{4}^{2+}$	2.126	2.077	1.956	0.169	2.053
$\mathbf{5}^{2+}$	2.141	2.089	1.948	0.192	2.059
$\mathbf{6}^{2+}$	2.149	2.089	1.943	0.206	2.060

[a]All data was recorded at 120 K in 0.1 M Bu_4NPF_6 acetonitrile electrolyte following room temperature controlled potential electrolysis.

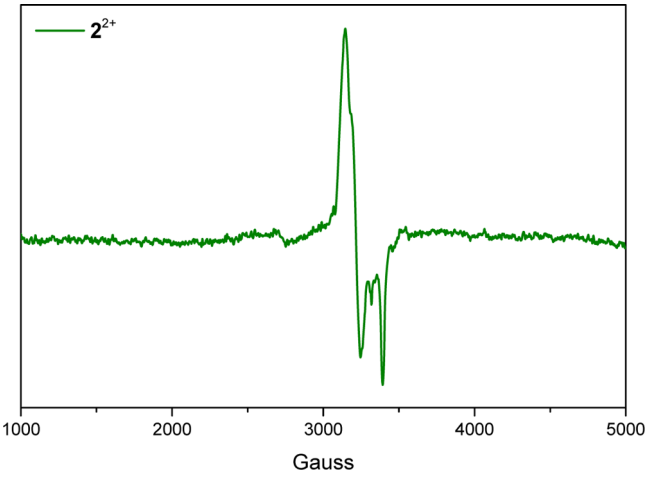

Figure 8. X-band EPR spectroelectrochemical data for complex $\mathbf{2}^{2+}$ recorded at 120 K following room temperature electrolysis at +0.55 V versus SCE in 0.1 M Bu_4NPF_6 acetonitrile electrolyte.

The *g*-anisotropy value ($\Delta g = g_x - g_z$) is also strongly influenced by the spin contribution of heavy atoms and provides a means to distinguish between metal and ligand centered radical character.[42,43] With the trend in Δg across the series $\mathbf{2}^{2+}$−$\mathbf{6}^{2+}$, it is possible to identify the predominant resonance form contributing to the one-electron oxidized species (Scheme 2). The F_4(MeO)Ph−CAQN complex $\mathbf{6}^{2+}$ displays the largest *g*-anisotropy of Δg = 0.206 from the R-CAQN series consistent with the weakest donating strength of

DOI: 10.1021/acs.inorgchem.5b02834
Inorg. Chem. XXXX, XXX, XXX−XXX

this ligand due to its extensive fluorination. In contrast, the electron donating tolyl substituent gives rise to the lowest *g*-anisotropy of the series with $\Delta g = 0.159$ implying the greatest Ru(II)-CAQN$^{\bullet}$ character for $\mathbf{2}^{2+}$. Relative to our prior EPR studies of isoelectronic oxyquinolate $[Ru(bpy)(R\text{-}OQN)]^{2+}$ complexes,[8,9] the range of *g* anisotropies here observed is quite narrow, and the values are also consistently low in value relative to that of the metal centered Ru(d^5) radical in $\mathbf{1}^{3+}$ ($\Delta g = 1.500$).[41] Thus, while rhombic anisotropy confirms the Ru(III) contribution to the singly occupied HOMO(α) level, the low *g*-anisotropies observed imply a majority contribution from the Ru(II)-CAQN$^{\bullet}$ resonance form across the $\mathbf{2}^{2+}$–$\mathbf{6}^{2+}$ series. This trend observed for fluorination versus hole delocalization across the Ru($d\pi$)-CAQN(π) framework is further corroborated by computational Mulliken spin-density analysis as illustrated in Figure 9. The calculated Mulliken spin-

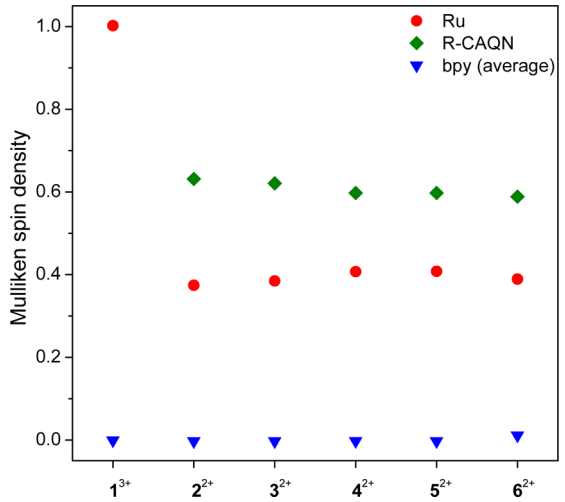

Figure 9. Mulliken spin-density analysis illustrating hole-delocalization onto the R-CAQN ligands of complexes $\mathbf{2}^{2+}$–$\mathbf{6}^{2+}$, relative to the spin-localized $\mathbf{1}^{3+}$ metallo-radical. Spin-density on the bpy ligands is presented as an average value.

density is located entirely on Ru(III) for $\mathbf{1}^{3+}$ which drops dramatically to 37% for $\mathbf{2}^{2+}$ with the remaining 63% located on the tolyl-CAQN ligand. This implies a majority Ru(II)-(tolyl-CAQN$^{\bullet}$) contribution according to Scheme 2, consistent with EPR analysis. A minimum calculated R-CAQN based Mulliken spin-density of 59% is observed for the least electron donating F_4(MeO)Ph–CAQN ligand complex $\mathbf{6}^{2+}$ consistent with it displaying the highest isotropic *g*-factor ($\langle g \rangle = 2.060$) and *g*-anisotropy ($\Delta g = 0.206$) of the Ru(R-CAQN) series.

Spectroelectrochemistry: Electronic Absorption Spectroscopy. Transition metal($d\pi$)–NIL(π) systems have a tendency to show strong NIR electronic transitions when containing NIL radical character. This is especially true of *o*-semiquinone, *o*-iminosemiquinone, and *o*-diiminosemiquinone complexes.[44] Previous spectroelectrochemical UV–vis–NIR studies of $[Ru(bpy)(R\text{-}OQN)]^{2+}$ complexes showed a strong NIR electronic transition whose maximum absorption and oscillator strength increased with increasing NIL radical character.[9] On the basis of this premise and consistent with computational, electrochemical, and EPR data presented above, a similar trend was anticipated for the isoelectronic $[Ru(bpy)(R\text{-}CAQN)]^{2+}$ series here under investigation. Sure enough, upon one-electron oxidation, strong in situ electrochromic changes were observed for the paramagnetic complexes $\mathbf{2}^{2+}$–$\mathbf{6}^{2+}$ across the entire UV–vis–NIR spectral range. An example of electrochromic transformation of $\mathbf{2}^{+}$ to $\mathbf{2}^{2+}$ under controlled potential electrolysis conditions is presented in Figure 10 with an accompanying molecular orbital diagram for both redox states.

Isosbestic points are observed at 304 and 327 nm confirming a clean transformation from $\mathbf{2}^{+}$ to $\mathbf{2}^{2+}$. Concurrent with the loss of major visible absorptions for the parent $\mathbf{2}^{+}$ complex is the growth of strong vis–NIR absorption bands at 392, 577, and 927 nm for $\mathbf{2}^{2+}$. The lowest energy absorption band at 927 nm (10 787 cm^{-1}) is particularly impressive stretching across a 400 nm range with a full width half-maximum of $\Delta\nu_{1/2} = 2010\ cm^{-1}$ and a molar extinction coefficient of $\varepsilon = 20\,750\ M^{-1}\ cm^{-1}$. The NIR absorption of $\mathbf{2}^{2+}$ consists of an almost equal mixture of two electronic transitions: (i) metal–ligand π–π^* [HOMO(β) → LUMO(β)] and (ii) metal-to-(metal–ligand) charge-transfer [MMLCT; HOMO−2(β) → LUMO(β)]. The latter MMLCT transition can be anticipated on the basis of a major resonance structure, in this case Ru(II)-CAQN$^{\bullet}$, originating from the primarily metal based HOMO − 2(β) orbital and populating the hybrid LUMO(β) energy level. Although some structural reorganization is observed in the DFT optimized geometry of $\mathbf{2}^{2+}$, most obvious in the reduced bpy/tolyl π-stacking, close inspection of the MO surfaces in Figure 9 allows assignment of the antibonding Ru($d\pi$)–CAQN(π) LUMO(β) orbital as the "electron–hole" of the paramagnetic complex seeing how it correlates to the HOMO surface of the diamagnetic $\mathbf{2}^{+}$ redox state. Also noteworthy is destabilization of the bonding Ru($d\pi$)–CAQN(π) HOMO(β) orbital of $\mathbf{2}^{2+}$, which correlates to the HOMO − 3 level of $\mathbf{2}^{+}$. This destabilization upon one-electron oxidation is most likely due to reduced π-donation of the CAQN$^{\bullet}$ ligand. Consistent with EPR and Mulliken spin-density analysis, where increased fluorination increases contribution from the Ru(III)-CAQN metalloradical resonance form, the oscillator strength of this NIR transition decreases accordingly until for $\mathbf{6}^{2+}$ it is barely visible with a molar extinction coefficient decreased by 2 orders of magnitude ($\varepsilon = 500\ M^{-1}\ cm^{-1}$, Figure 11).

COMPARISON WITH RELATED NONINNOCENT LIGANDS

Finally, it is worth considering the electronic properties of $[Ru(bpy)_2(R\text{-}CAQN)]^{+}$ complexes against related ruthenium polypyridyl noninnocent ligand (NIL) complexes to gauge where R-CAQN lies on the spectrum of noninnocent versus classical redox-active metal–ligand combinations. For this purpose $\mathbf{2}^{+}$ with the simple tolyl-CAQN ligand is used, and as above, $\mathbf{1}^{2+}$ is used as the innocent redox-active reference. The isolectronic 8-oxyquinolate (OQN) ligand previously studied by our group[8] is also included as well as the popular *o*-semiquinone [(O,O)SQ], *o*-aminosemiquinone [(NH,O)SQ], and *o*-diaminosemiquinone [(NH,NH)SQ] series of ligands (Figure 12).[3,45]

Table 5 summarizes data for the first oxidation potential of all complexes as well as the EPR determined isotropic *g*-factors and DFT calculated Mulliken spin-densities. Note that all three $[Ru(bpy)_2(NIL)]^{+}$ semiquinone complexes are paramagnetic and EPR active in their native 1+ redox states. Although all of the noninnocent ligands compared in Table 5 (excluding bpy of course) carry a formal charge of −1 there is a distinct difference in their oxidation potentials which occur over a relatively large range of 0.84 V. A simple Coulombic explanation is insufficient

DOI: 10.1021/acs.inorgchem.5b02834
Inorg. Chem. XXXX, XXX, XXX–XXX

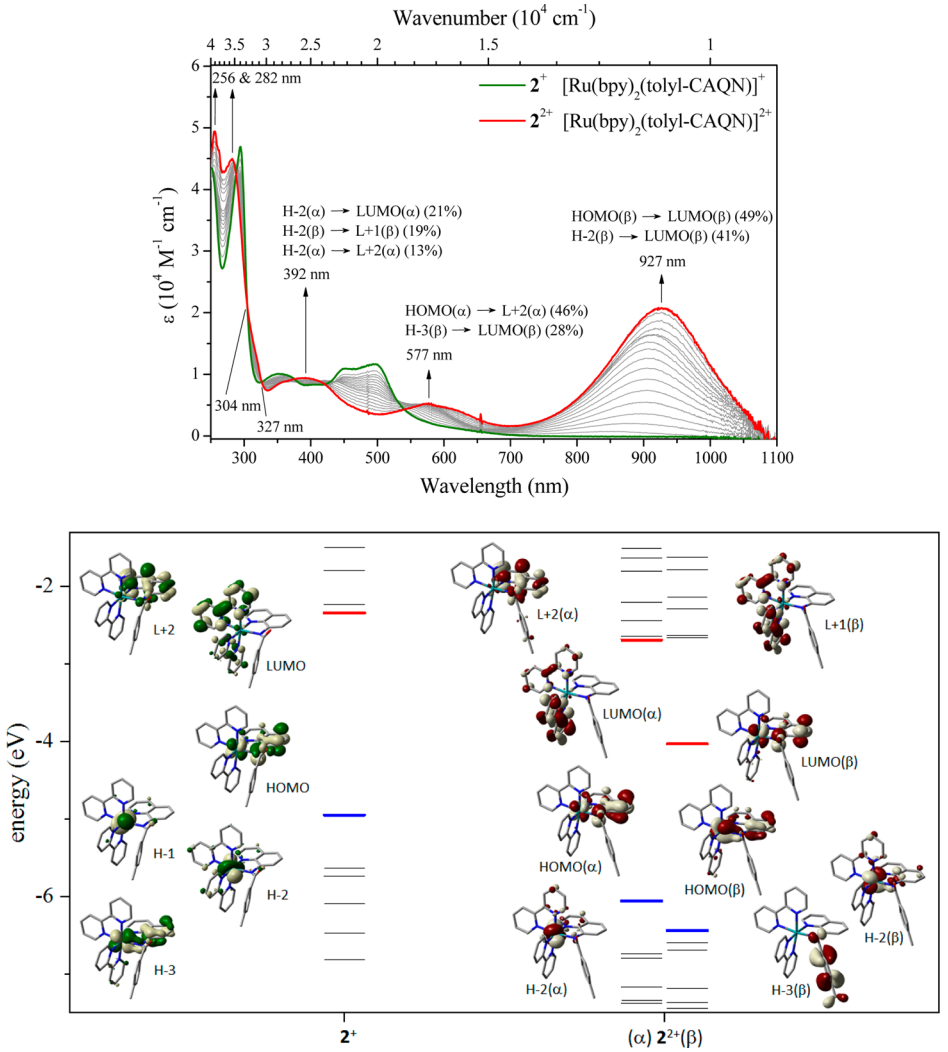

Figure 10. (Top) Overlay of UV−vis−NIR absorption spectra for the spectroelectrochemical conversion of [Ru(bpy)$_2$(tolyl-CAQN)]$^+$ to its one-electron oxidized derivative [Ru(bpy)$_2$(tolyl-CAQN)]$^{2+}$. Evolution of new experimental absorption maxima and isosbestic points (304 and 327 nm) is highlighted alongside majority TDDFT assignments. All spectra were recorded in 0.1 M Bu_4NPF_6 acetonitrile electrolyte at room temperature under controlled potential electrolysis conditions at an applied bias of +0.55 V versus SCE. (Bottom) Molecular orbital correlation diagram for $\mathbf{2}^+$ and $\mathbf{2}^{2+}$ (left = α orbitals, right = β orbitals) including select frontier molecular orbital surfaces (isofactor = 0.04).

to explain this range of redox potentials. This is best understood in terms of the so-called noninnocent ligand effect which is essentially a variance in the extent of metal−ligand π-bonding (vide supra). More specifically, trends in the observed first oxidation redox couples can be rationalized by the relative energy alignment of NIL frontier π-orbitals with the bonding Ru atomic d-orbitals in both redox states of the complex, i.e., [Ru(bpy)$_2$(NIL)]$^{n+}$, where n = +2 and +1. All three semiquinone complexes have been previously characterized by Lever and co-workers who established that the radical charge is primarily located on the NIL fragment.[45] This is consistent with their low isotropic g-factors (1.997−2.000) characteristic of an organic radical and the high spin-density calculated on the NIL fragment (84−86%). Both *o*-aminosemiquinone [(NH,O)-SQ] and *o*-diaminosemiquinone [(NH,NH)SQ] complexes appear to have high lying SOMO levels due to their ease of oxidation at +0.05 and −0.45 V versus SCE, respectively. This is consistent with each of their N atoms carrying significant radical character[46] and is in stark contrast to the *o*-semiquinone [(O,O)SQ] complex which is oxidized at +0.56 V versus SCE, slightly positive of the tolyl-CAQN ($\mathbf{1}^+$) and OQN complexes. The tolyl-CAQN redox potential ($\mathbf{1}^{2+/+}$) occurs intermediate between the (O,O)SQ and (NH,O)SQ complexes which is consistent with partial Ru(III) character evident by its rhombic EPR spectrum, increased g-factor (2.048), and 37% calculated Mulliken spin-density at the metal center. In comparison, the [Ru(bpy)$_2$(OQN)]$^{2+}$ complex carries a greater percentage of Ru(III) character in its SOMO level consistent with it having the highest g-factor (2.120) of the NIL series here compared. Thus, the R-CAQN class of ligands can be considered its own class of NIL alongside its OQN and *o*-semiquinone counterparts, at least when coordinated to Ru(II), with the advantage of having a greater scope for synthetic variation and fine-tuning of its properties as described above for the $\mathbf{2}^+$−$\mathbf{6}^+$ series of complexes.

CONCLUSIONS

In summary, a series of bis-heteroleptic ruthenium(II) bis-bipyridyl *N*-(carboxyaryl)amidoquinolate complexes are presented with varying degrees of *N*-carboxyaryl fluorination. X-ray crystallography confirms a favorable π-stacking of the *N*-carboxyaryl substituent of the CAQN ligand with the adjacent

DOI: 10.1021/acs.inorgchem.5b02834
Inorg. Chem. XXXX, XXX, XXX−XXX

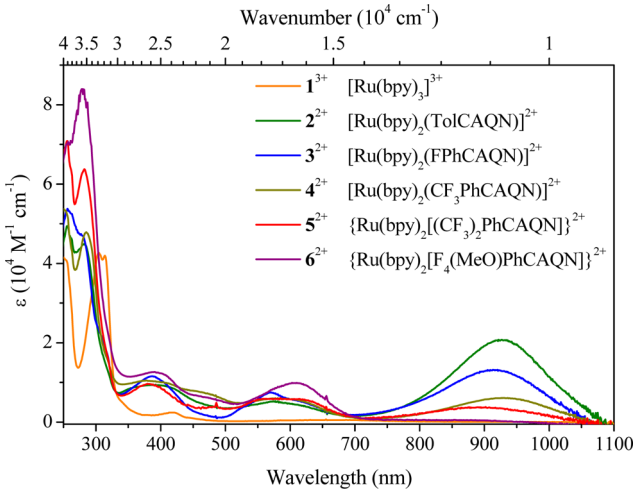

Figure 11. Overlay of UV−vis absorption spectra for the one-electron oxidized derivatives $\mathbf{1}^{3+}$−$\mathbf{6}^{2+}$. All spectra were recorded in 0.1 M Bu_4NPF_6 acetonitrile electrolyte at room temperature following controlled potential electrolysis.

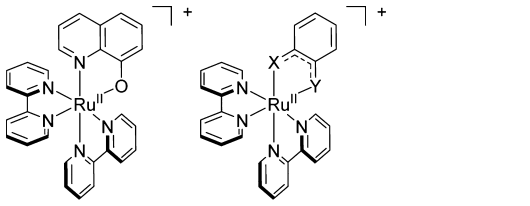

Figure 12. Structures of the previously reported $[Ru(bpy)_2(NIL)]^+$ complexes where the noninnocent ligand (NIL) = 8-oxyquinolate (OQN), *o*-semiquinone [(O,O)SQ], *o*-aminosemiquinone [(NH,O)-SQ], and *o*-diaminosemiquinone [(NH,NH)SQ].

Table 5. Summary of Electronic Properties for a Series of Isoelectronic $[Ru(bpy)_2(NIL)]^{2+}$ Complexes (Where NIL = Bidentate Noninnocent Ligand) Including $\mathbf{1}^{3+}$, $\mathbf{2}^{2+}$, and Related Semiquinone Complexes

	E_{Ox}[a]	⟨*g*⟩	Ru/NIL Mulliken spin-density
$\mathbf{1}^{2+}$	+1.29	2.140[b]	100/0[b]
$\mathbf{2}^{+}$	+0.37	2.048[b]	37/63[b]
OQN[8]	+0.52	2.120[b]	46/54[b]
(O,O)SQ[45]	+0.56	2.000[c]	16/86[d]
(NH,O)SQ[45]	+0.05	2.000[c]	17/84[d]
(NH,NH)SQ[45]	−0.47	1.997[c]	12/88[d]

[a]All redox potentials were recorded in 0.1 M Bu_4NPF_6 acetonitrile electrolyte and are reported vs SCE. [b]Data obtained for one-electron oxidized species [c]Recorded at 100 K in dichloroethane. [d]Calculated using the B3LYP exchange-corellation functional with the TZVP (Ru) and DGDZVP (C,H,N,O) basis sets.[46]

bpy ligand at the ruthenium center. Spectroelectrochemical EPR and UV−vis−NIR spectroscopies show complementary results to DFT analysis supporting the presence of a noninnocent Ru(dπ)−CAQN(π) bonding interaction, which is responsible for enhanced light harvesting and redox tunability of these complexes. The noninnocent Ru(dπ)−CAQN(π) interaction imparts a strong influence on the complex electronic structure where both the UV and visible regions of their absorption spectra are dominated by ^{1}MLLCT absorption bands with major contributions from [Ru(dπ)-CAQN(π)] → CAQN(π*) type transitions (Figure 3). While fluorination of the *N*-carboxyaryl substituent does not have a strong influence on the absorption spectra, the first oxidation potential is tuned over a range of 0.92 V with respect to $\mathbf{1}^{2+}$. EPR and Mulliken spin-density analyses of the one-electron oxidized complexes confirm that an increased contribution of the CAQN ligand to the HOMO level occurs with decreased fluorination. Combination of ruthenium based redox stability with the strong CAQN light harvesting properties is a highly attractive feature of the noninnocent Ru(dπ)−CAQN(π) system, which also offers a great scope for synthetic variation and electronic tuning relative to related OQN and *o*-semiquinone systems. Future studies will take advantage of these properties for application in photovoltaic and catalysis applications.

EXPERIMENTAL SECTION

Physical Measurements. UV−vis−NIR absorption spectra were recorded on an Agilent 8453 diode array spectrophotometer in spectrophotometric grade acetonitrile. NMR spectra were recorded on an Agilent spectrometer operated at 399.80 MHz for ^{1}H, 100.54 MHz for ^{13}C, and 376.15 MHz for ^{19}F. Deuterated solvents *d*-chloroform, d_6-acetone, and d_6-dimethyl sulfoxide were used as received from Aldrich and their residual ^{1}H solvent signals (δ = 7.26, 2.05, and 2.50 ppm respectively) used as internal references for reporting the ^{1}H chemical shift (δ).[47] Likewise, the ^{13}C signal of d_6-dimethyl sulfoxide (δ = 39.52 ppm) was used as an internal reference for reporting ^{13}C NMR spectra. Trifluoroethanol (δ ($CDCl_3$) = −77.00 ppm) was used as an external standard for referencing ^{19}F chemical shifts in deuterated d_6-acetone (δ = −77.44 ppm) and d_6-dimethyl sulfoxide (δ = −75.07 ppm). LC−MS of ligands L5−L7 was performed on an Agilent 2100 system using atmospheric pressure chemical ionization (APCI) mode. Mobile phases consisted of methanol and water both containing 0.05% trifluoroacetic acid. A linear gradient was used to increase from 25:75 v/v methanol/water to 100% methanol over 7.0 min at a flow rate of 0.7 mL/min with a C18 (5.0 μm, 6.0 mm × 50 mm) column. UV detection of the eluent was conducted at 210, 254, and 365 nm. ESI-MS was carried out on a Thermo Finnigan mass spectrometer. Elemental analysis was conducted with a PerkinElmer 2400 instrument. Cyclic voltammetry was carried out on a CH Instruments 620D potentiostat. A standard three electrode cell was used under an atmosphere of argon with 0.1 M Bu_4NPF_6 in spectrophotometric grade acetonitrile as supporting electrolyte. Glassy carbon (3 mm diameter) and Pt wire were used as working and counter electrodes, respectively. A nonaqueous reference electrode was used to minimize ohmic potential drop at the solvent interface. This consisted of a Ag wire in 0.1 M Bu_4NPF_6 acetonitrile supporting electrolyte isolated by a vycor frit and was calibrated using the ferricenium/ferrocene redox couple as a pseudoreference (+0.45 V vs SCE).[48] Redox potentials (E) were determined from cyclic voltammetry as $(E_{pa} + E_{pc})/2$, where E_{pa} and E_{pc} are the anodic and cathodic peak potentials, respectively. Where E could not be calculated due to irreversible behavior, E_{pc} or E_{pa} are reported accordingly. For controlled potential electrolysis experiments, Pt gauze electrodes were used as both working and counter electrodes with the counter electrode isolated via a fine porosity vycor frit. UV−vis−NIR spectroelectrochemical experiments were conducted with a custom spectroelectrochemical flow cell whose design is based upon a literature description.[49] EPR spectra were recorded on a Bruker Elexys E500 spectrometer at 120 K with an X-band microwave source.

Computational Details. All calculations were carried out using density functional theory (DFT) with the B3LYP functional and acetonitrile polarizable continuum model (PCM)[50] as implemented in the Gaussian 09 B.01 program package.[51] The LANL08 relativistic effective core potential (RECP) basis set was used for Ru[52] and 6-31G(d,p)[53,54] for C, H, N, O, F. A vibrational frequency analysis was carried out in order to confirm the minimum-energy geometry and

DOI: 10.1021/acs.inorgchem.5b02834
Inorg. Chem. XXXX, XXX, XXX−XXX

determine the zero-point energy for each species; i.e., geometry optimization and frequency calculations were performed for both the native $\mathbf{1}^{2+}$–$\mathbf{6}^{+}$ complexes and their one-electron oxidized derivatives $\mathbf{1}^{3+}$–$\mathbf{6}^{2+}$. Electronic transitions ($N = 60$) were calculated in acetonitrile with the PCM optimized geometry using time-dependent density functional theory (TDDFT)[55] at the same level of theory. Successful implementation of these DFT/TDDFT parameters has proven successful in the past for ruthenium polypyridyl complexes.[56]

Collection and Reduction of X-ray Data. A crystal (0.50 × 0.20 × 0.13 mm^3) of $\mathbf{2}(PF_6)\cdot 0.125H_2O$ was mounted on the end of a glass fiber and transferred to Bruker Kappa Apex II diffractometer for the collection of diffraction data. Diffraction data indicated monoclinic symmetry and systematic absences consistent with space group $P2/n$. Crystal data and information about the data collection are provided in the Supporting Information.

Determination and Refinement of the Structure. The structure of $\mathbf{2}(PF_6)\cdot 0.125H_2O$ was solved by direct methods.[57] There are two molecules of $\mathbf{2}(PF_6)\cdot 0.125H_2O$ in the symmetry unit. A disordered model was used for the hexafluorophosphate ions, and the occupancy factor of the water of crystallization was refined to 0.129(8). In the least-squares refinement,[57] anisotropic temperature parameters were used for all the non-hydrogen atoms except for the fluorine and oxygen atoms of the disordered hexafluorophosphate and water with occupancy factors less than 0.5. Hydrogen atoms were placed at calculated positions and allowed to "ride" on the atom to which they were attached except for the hydrogen atoms on the water of crystallization which were not included. The isotropic thermal parameter for the hydrogen atoms were determined from the atom to which they were attached. The data was corrected using the multiscan method (SADABS).[58]

Synthetic Procedures. *Materials.* 8-Aminoquinoline, toluoyl chloride, 4-methoxy-2,3,5,6-tetrafluorobenzoyl chloride, triethylamine, tetrabutylammoniumhydroxide (0.1 M in methanol), potassium hexafluorophosphate, and spectroscopic grade acetonitrile were purchased from Aldrich and used as received. 4-Fluorobenzoyl chloride, 4-trifluoromethylbenzoyl chloride, 3,5-bis(trifluoromethyl)-benzoyl chloride, and pentafluorobenzoyl chloride were purchased from Oakwood Chemicals and used as received. Reagent grade dichloromethane, methanol, acetone, and diethyl ether were purchased from Pharmco Aaper and used as received. Tetrabutyl ammonium hexafluorophosphate (Aldrich) was recrystallized thrice from hot ethanol and dried under vacuum prior to use. The complexes $Ru(bpy)_2Cl_2$[59] and $[Ru(bpy)_3](PF_6)_2$[60] were prepared according to the literature. Ligands *N*-(carboxy-4-tolyl)-8-aminoquinoline (L2),[24] *N*-(carboxy-4-fluorophenyl)-8-aminoquinoline (L3),[24] and *N*-(carboxy-4-trifluoromethylphenyl)-8-aminoquinoline (L4)[61] were synthesized as described below, and their analytical data was consistent with those reported previously.

General Procedure for Synthesis of N-Carboxyaryl-8-aminoquinoline (R-CAQN·H) Ligands. To a 5 mL solution of dry CH_2Cl_2 under an argon atmosphere was added sequentially 8-aminoquinoline (0.432 g, 3 mmol) and Et_3N (0.43 mL, 3.1 mmol). The appropriate benzoyl chloride (3 mmol) was then added dropwise if liquid or directly if a solid. The resulting mixture was stirred at room temperature for 1 h maintaining an argon atmosphere. The dark brown solution was then transferred to a separating funnel and washed with water, sat. $NaHCO_3$, and brine. The organic layer was dried over $MgSO_4$, and the solvent was removed under reduced pressure. Typically a pale brown solid or oil was recovered. In all cases analytically pure compound was obtained in 70–80% yield by recrystallization from a concentrated dichloromethane solution by addition of excess hexanes.

*N-(Carboxy-3,5-bis(trifluoromethyl)phenyl)-8-aminoquinoline (**L5**).* ^{1}H NMR $\delta[(CD_3)_2SO]$: 7.65–7.70 (m, 2H), 7.83 (dd, 1H, J = 1.2, 8.0 Hz), 8.42 (s, 1H), 8.47 (dd, 1H, J = 1.6, 8.0 Hz), 8.55 (dd, 1H, J = 1.20, 8.0 Hz), 8.65 (s, 2H), 8.99 (dd, 1H, J = 1.6, 4.0 Hz), 10.94 (s, 1H) ppm. ^{13}C NMR $\delta[(CD_3)_2SO]$: 109.56, 119.64, 121.75, 122.27, 123.82, 125.36, 126.77, 128.05, 128.41, 130.49, 130.82, 133.86, 136.67, 137.16, 139.48, 144.80, 149.51, 162.69 ppm. ^{19}F NMR $\delta[(CD_3)_2SO]$: −61.00 (s) ppm. LC–MS (m/z): calcd (M + 1) 385.1; obsd 385.1.

*N-(Carboxy-2,3,5,6-tetrafluoro-4-methoxyphenyl)-8-aminoquinoline (**L6**).* ^{1}H NMR $\delta[(CD_3)_2SO]$: 4.13 (t, 3H, J = 1.5 Hz), 7.64–7.68 (m, 2H), 7.80 (dd, 1H, J = 1.2, 8.0 Hz), 8.46 (dd, 1H, J = 1.6, 8.0 Hz), 8.70 (dd, 1H, J = 0.8, 8.0 Hz), 8.94 (dd, 1H, J = 1.6, 4.0 Hz), 11.03 (s, 1H) ppm. ^{13}C NMR $\delta[(CD_3)_2SO]$: 45.60, 117.89, 122.35, 123.54, 126.87, 127.95, 133.75, 136.65, 138.37, 149.28, 156.36 ppm. ^{19}F NMR $\delta[(CD_3)_2SO]$: −143.36 (m), −157.46 (m) ppm. LC–MS (m/z): calcd (M + 1) 351.1; obsd 351.1.

*N-(Carboxy-perfluorophenyl)-8-aminoquinoline (**L7**).* ^{1}H NMR $\delta[(CD_3)_2SO]$: 7.65–7.69 (m, 2H), 7.82 (dd, 1H, J = 1.2, 8.0 Hz), 8.46 (dd, 1H, J = 2.0, 8.0 Hz), 8.70 (dd, 1H, J = 1.2, 8.0 Hz), 8.94 (d, 1H, J = 4.5 Hz), 11.20 (s, 1H) ppm. ^{13}C NMR $\delta[(CD_3)_2SO]$: 118.21, 122.38, 123.82, 126.86, 128.00, 133.66, 136.68, 138.47, 149.36, 155.75 ppm. ^{19}F NMR $\delta[(CD_3)_2SO]$: −141.87 (m), −153.09 (t), −161.77 (m) ppm. LC–MS (m/z): calcd (M + 1) 339.1; obsd 339.1.

General Synthetic Method for [Ru(bpy)$_2$(R-CAQN)](PF$_6$) Complexes. A 50 mL flask was charged with 10 mL of methanol and the solution purged with argon for 10 min. The flask was charged with 0.10 mmol of $Ru(bpy)_2Cl_2$, 0.11 mmol of the appropriately substituted *N*-(arylcarboxy)-8-aminoquinoline ligand and 1.1 mL of 0.1 M aqueous tetrabutylammonium hydroxide. Maintaining an argon atmosphere the purple suspension was allowed to reflux with stirring for 5 h resulting in a deep reddish/brown solution. The methanol was then removed on a rotary evaporator resulting in a crude aqueous solution of the $[Ru(bpy)_2(R\text{-}CAQN)]Cl$ salt. Additional water was added (5 mL), and any unreacted ligand was removed by gravity filtration. To the deep red homogeneous filtrate was added dropwise 1 M aqueous KPF_6 until a dark red precipitate developed. The solid was isolated by vacuum filtration on a medium porosity sintered funnel. Recrystallization from acetone and diethyl ether gave analytically pure product in 70–80% yield.

*[Ru(bpy)$_2$(Tolyl-CAQN)](PF$_6$) (**2**$^+$).* ^{1}H NMR $\delta[(CD_3)_2CO]$: 2.14 (s, 3H), 6.52 (d, 2H, J = 7.6 Hz), 6.59 (s, 2H), 7.02–7.06 (m, 1H), 7.21–7.25 (m, 1H), 7.32–7.40 (m, 2H), 7.49 (d, 2H, J = 5.2 Hz), 7.54–7.57 (m, 1H), 7.61–7.71 (m, 3H), 7.75 (d, 1H, J = 5.2 Hz), 7.98 (ddd, 1H, J = 0.4, 1.6, 8.0 Hz), 8.03 (ddd, 1H, J = 0.4, 1.6, 8.0 Hz), 8.11–8.21 (m, 5H), 8.53–8.59 (m, 3H), 9.27 (d, 1H, J = 5.2 Hz) ppm. ^{19}F NMR $\delta[(CD_3)_2CO]$: −72.39 (d, J = 707 Hz) ppm. ESI-MS [m/z ($-PF_6^-$)]: calcd 675.1; obsd 675.1. Anal. Calcd for $C_{37}H_{29}F_6N_6OPRu$: C, 54.21; H, 3.57; N, 10.25. Found: C, 54.11; H, 3.70; N, 10.11.

*[Ru(bpy)$_2$(F-CAQN)](PF$_6$) (**3**$^+$).* ^{1}H NMR $\delta[(CD_3)_2CO]$: 6.48 (dd, 2H, J = 8.8, 8.8 Hz), 6.77 (s, 2H), 7.08 (ddd, 1H, J = 1.6, 3.2, 6.4 Hz), 7.24 (dd, 1H, J = 3.2, 4.8 Hz), 7.33–7.41 (m, 2H), 7.51–7.59 (m, 3H), 7.61–7.73 (m, 3H), 7.77 (d, 1H, J = 6.0 Hz), 8.00 (ddd, 1H, J = 0.8, 1.6, 8.4 Hz), 8.05 (ddd, 1H, J = 0.8, 1.6, 8.4 Hz), 8.12–8.23 (m, 5H), 8.57–8.59 (m, 3H), 9.27 (d, 1H, J = 5.4 Hz) ppm. ^{19}F NMR $\delta[(CD_3)_2CO]$: −72.40 (d, J = 707 Hz), −113.68 (s) ppm. ESI-MS [m/z ($-PF_6^-$)]: calcd 679.1; obsd 679.1. Anal. Calcd for $C_{36}H_{26}F_7N_6OPRu$: C, 52.50; H, 3.18; N, 10.20. Found: C, 52.26; H, 3.28; N, 10.08.

*[Ru(bpy)$_2$(CF$_3$Ph-CAQN)](PF$_6$) (**4**$^+$).* ^{1}H NMR $\delta[(CD_3)_2CO]$: 6.88 (s, 2H), 7.01–7.05 (m, 3H), 7.25 (dd, 1H, J = 4.8, 8.0 Hz), 7.36–7.40 (m, 1H), 7.42 (dd, 1H, J = 1.2, 8.0 Hz), 7.51 (ddd, 1H, J = 0.8, 1.2, 6.4 Hz), 7.55–7.59 (m, 2H), 7.62–7.67 (m, 2H), 7.72 (dd, 1H, J = 1.2, 5.2 Hz), 7.74 (ddd, 1H, J = 0.8, 1.2, 5.6 Hz), 8.01 (ddd, 1H, J = 0.8, 1.2, 12 Hz), 8.07 (ddd, 1H, J = 0.4, 1.2, 12 Hz), 8.15–8.19 (m, 3H), 8.25 (dd, 1H, J = 1.6, 8.4 Hz), 8.51 (dd, 1H, J = 1.2, 8.0 Hz), 8.56–8.61 (m, 3H), 9.23 (ddd, 1H, J = 0.8, 1.6, 6.0 Hz) ppm. ^{19}F NMR $\delta[(CD_3)_2CO]$: −62.85 (s), −72.43 (d, J = 711 Hz) ppm. ESI-MS [m/z ($-PF_6^-$)]: calcd 729.1; obsd 729.1. Anal. Calcd for $C_{37}H_{26}F_9N_6OPRu$: C, 50.87; H, 3.00; N, 9.62. Found: C, 50.62; H, 3.06; N, 9.48.

*[Ru(bpy)$_2$(CF$_3$)$_2$Ph-CAQN](PF$_6$) (**5**$^+$).* ^{1}H NMR $\delta[(CD_3)_2CO]$: 7.00 (ddd, 1H, J = 0.8, 1.6, 13.6 Hz), 7.28 (dd, 1H, J = 5.2, 8.4 Hz), 7.30–7.45 (m, 3H), 7.48 (dd, 1H, J = 1.2, 8.0 Hz), 7.51 (ddd, 1H, J = 0.8, 1.6, 5.6 Hz), 7.56–7.63 (m, 3H), 7.65–7.71 (m, 3H), 7.75 (dd, 1H, J = 1.6, 4.8 Hz), 8.02 (ddd, 1H, J = 0.8, 1.6, 16.0 Hz), 8.10 (ddd, 1H, J = 0.8, 1.6, 16.0 Hz), 8.13–8.20 (m, 2H), 8.23 (d, 1H, J = 7.2 Hz), 8.29 (dd, 1H, J = 1.6, 8.4 Hz), 8.47 (dd, 1H, J = 1.6, 8.4 Hz), 8.58–8.64 (m, 3H), 9.33 (ddd, 1H, J = 0.8, 1.6, 16.0 Hz) ppm. ^{19}F NMR

DOI: 10.1021/acs.inorgchem.5b02834
Inorg. Chem. XXXX, XXX, XXX–XXX

δ[$(CD_3)_2CO$]: −62.97 (s), −72.42 (d, J = 707 Hz) ppm. ESI-MS [m/z ($-PF_6^-$)]: calcd 797.1; obsd 797.1. Anal. Calcd for $C_{38}H_{25}F_{12}N_6OPRu$: C, 48.47; H, 2.68; N, 8.92. Found: C, 48.24; H, 2.88; N, 8.81.

*{Ru(bpy)$_2$[F$_4$(MeO)Ph-CAQN]}(PF$_6$) (**6**$^+$).* ^{1}H NMR δ[$(CD_3)_2CO$]: 3.95 (t, 3H, J = 1.5 Hz), 7.20 (ddd, 1H, J = 1.2, 5.6, 7.2 Hz), 7.28 (dd, 1H, J = 4.8, 8.0 Hz), 7.39 (ddd, 1H, J = 1.2, 6.4, 7.2 Hz), 7.54 (ddd, 1H, J = 1.2, 6.6, 7.6 Hz), 7.59 (dd, 1H, J = 1.2, 8.0 Hz), 7.64−7.70 (m, 4H), 7.75 (dd, 1H, J = 1.2, 4.8 Hz), 7.84 (ddd, 1H, J = 0.8, 1.6, 7.2 Hz), 8.01−8.09 (m, 2H), 8.14 (ddd, 1H, J = 0.8, 1.2, 5.6 Hz), 8.19 (ddd, 1H, J = 0.8, 1.2, 5.6 Hz), 8.30 (dd, 1H, J = 1.2, 8.0 Hz), 8.46 (d, 1H, J = 8.0 Hz), 8.57−8.61 (m, 2H), 8.69 (d, 1H, J = 8.0 Hz), 9.01 (m, 1H), 9.45 (s, 1H) ppm. ^{19}F NMR δ[$(CD_3)_2CO$]: −72.43 (d, J = 707 Hz), −143.96 (m), −147.14 (m), 157.43 (m), 158.29 (m) ppm. ESI-MS [m/z ($-PF_6^-$)]: calcd 763.1; obsd 763.1. Anal. Calcd for $C_{37}H_{25}F_{10}N_6O_2PRu$: C, 48.96; H, 2.78; N, 9.26. Found: C, 48.70; H, 2.85; N, 9.18.

■ ASSOCIATED CONTENT

Supporting Information

The Supporting Information is available free of charge on the ACS Publications website at DOI: 10.1021/acs.inorgchem.5b02834.

NMR and MS spectra, crystallographic parameters, TDDFT data and Cartesian coordinates, and complete ref 51 (PDF)

Crystallographic data (CIF)

■ AUTHOR INFORMATION

Corresponding Author

*E-mail: jonathan.rochford@umb.edu.

Author Contributions

The manuscript was written through contributions of all authors. All authors have given approval to the final version of the manuscript.

Notes

The authors declare no competing financial interest.

■ ACKNOWLEDGMENTS

We thank Dr. E. Fujita of Brookhaven National Laboratory for the use of the Bruker Kappa Apex II diffractometer for X-ray data collection.

■ REFERENCES

(1) Broere, D. L. J.; Plessius, R.; van der Vlugt, J. I. *Chem. Soc. Rev.* **2015**, *44*, 6886−6915.

(2) Luca, O. R.; Crabtree, R. H. *Chem. Soc. Rev.* **2013**, *42*, 1440−1459.

(3) Boyer, J. L.; Rochford, J.; Tsai, M. K.; Muckerman, J. T.; Fujita, E. *Coord. Chem. Rev.* **2010**, *254*, 309−330.

(4) Jørgensen, C. K. *Coord. Chem. Rev.* **1966**, *1*, 164−178.

(5) Karen, P. *Angew. Chem., Int. Ed.* **2015**, *54*, 4716−4726.

(6) Kaim, W. *Eur. J. Inorg. Chem.* **2012**, *2012*, 343−348.

(7) Ingram, J. D.; Costa, P. J.; Adams, H.; Ward, M. D.; Félix, V.; Thomas, J. A. *Inorg. Chem.* **2012**, *51*, 10483−10494.

(8) Zhao, H. C.; Fu, B.-L.; Schweinfurth, D.; Harney, J. P.; Sarkar, B.; Tsai, M.-K.; Rochford, J. *Eur. J. Inorg. Chem.* **2013**, *2013*, 4410−4420.

(9) Bellinger-Buckley, S.; Chang, T.-C.; Bag, S.; Schweinfurth, D.; Zhou, W.; Torok, B.; Sarkar, B.; Tsai, M.-K.; Rochford, J. *Inorg. Chem.* **2014**, *53*, 5556−5567.

(10) Mandal, A.; Grupp, A.; Schwederski, B.; Kaim, W.; Lahiri, G. K. *Inorg. Chem.* **2015**, *54*, 10049−10057.

(11) Laine, T. M.; Karkas, M. D.; Liao, R.-Z.; Siegbahn, P. E. M.; Akermark, B. *Chem. - Eur. J.* **2015**, *21*, 10039−10048.

(12) Weisser, F.; Plebst, S.; Hohloch, S.; van der Meer, M.; Manck, S.; Führer, F.; Radtke, V.; Leichnitz, D.; Sarkar, B. *Inorg. Chem.* **2015**, *54*, 4621−4635.

(13) Robson, K. C. D.; Bomben, P. G.; Berlinguette, C. P. *Dalton Trans.* **2012**, *41*, 7814−7829.

(14) Radwan, Y. K.; Maity, A.; Teets, T. S. *Inorg. Chem.* **2015**, *54*, 7122−7131.

(15) Allu, S.; Swamy, K. C. K. *J. Org. Chem.* **2014**, *79*, 3963−3972.

(16) Begum, R. A.; Day, V. W.; Kumar, M.; Gonzalez, J.; Jackson, T. A.; Bowman-James, K. *Inorg. Chim. Acta* **2014**, *417*, 287−293.

(17) Harrop, T. C.; Olmstead, M. M.; Mascharak, P. K. *Inorg. Chem.* **2005**, *44*, 9527−9533.

(18) Zhang, S.-Y.; Li, Q.; He, G.; Nack, W. A.; Chen, G. *J. Am. Chem. Soc.* **2015**, *137*, 531−539.

(19) Liu, S.; Sun, W.-H.; Zeng, Y.; Wang, D.; Zhang, W.; Li, Y. *Organometallics* **2010**, *29*, 2459−2464.

(20) Wang, K.; Shen, M.; Sun, W.-H. *Dalton Trans.* **2009**, 4085−4095.

(21) Lee, J. C., Jr.; Peris, E.; Rheingold, A. L.; Crabtree, R. H. *J. Am. Chem. Soc.* **1994**, *116*, 11014−11019.

(22) Gregoliński, J.; Hikita, M.; Sakamoto, T.; Sugimoto, H.; Tsukube, H.; Miyake, H. *Inorg. Chem.* **2016**, *55*, 633−643.

(23) Begum, R. A.; Day, V. W.; Kumar, M.; Gonzalez, J.; Jackson, T. A.; Bowman-James, K. *Inorg. Chim. Acta* **2014**, *417*, 287−293.

(24) Lee, J. C.; Peris, E.; Rheingold, A. L.; Crabtree, R. H. *J. Am. Chem. Soc.* **1994**, *116*, 11014−11019.

(25) Roane, J.; Daugulis, O. *Org. Lett.* **2013**, *15*, 5842−5845.

(26) Wu, F.; Riesgo, E.; Pavalova, A.; Kipp, R. A.; Schmehl, R. H.; Thummel, R. P. *Inorg. Chem.* **1999**, *38*, 5620−5628.

(27) Philips, J. J.; Hudspeth, M. A.; Browne, P. M., Jr.; Peralta, J. E. *Chem. Phys. Lett.* **2010**, *495*, 146−150.

(28) Daul, C.; Baerends, E. J.; Vernooijs, P. *Inorg. Chem.* **1994**, *33*, 3538−3543.

(29) Kober, E. M.; Meyer, T. J. *Inorg. Chem.* **1982**, *21*, 3967−3977.

(30) Juris, A.; Balzani, V.; Barigelletti, F.; Campagna, S.; Belser, P.; Vonzelewsky, A. *Coord. Chem. Rev.* **1988**, *84*, 85−277.

(31) The actual point groups of $\mathbf{1}^{2+}$ and $\mathbf{2}^{+}$ are D_3 and C_1, respectively, if the peripheral ligand structures are considered. The *pseudo*-O_h and *pseudo*-C_s point groups are used here for simplicity.

(32) Damrauer, N. H.; Cerullo, G.; Yeh, A.; Boussie, T. R.; Shank, C. V.; McCusker, J. K. *Science* **1997**, *275*, 54−57.

(33) O'Donnell, R. M.; Johansson, P. G.; Abrahamsson, M.; Meyer, G. J. *Inorg. Chem.* **2013**, *52*, 6839−6848.

(34) Caspar, J. V.; Meyer, T. J. *J. Phys. Chem.* **1983**, *87*, 952−957.

(35) Muro-Small, M. L.; Yarnell, J. E.; McCusker, C. E.; Castellano, F. N. *Eur. J. Inorg. Chem.* **2012**, *2012*, 4004−4011.

(36) Nazeeruddin, M. K.; Kay, A.; Rodicio, I.; Humphrybaker, R.; Muller, E.; Liska, P.; Vlachopoulos, N.; Grätzel, M. *J. Am. Chem. Soc.* **1993**, *115*, 6382−6390.

(37) Biner, M.; Buergi, H. B.; Ludi, A.; Roehr, C. *J. Am. Chem. Soc.* **1992**, *114*, 5197−5203.

(38) Kaim, W.; Fiedler, J. *Chem. Soc. Rev.* **2009**, *38*, 3373−3382.

(39) Mondal, P.; Ray, R.; Das, A.; Lahiri, G. K. *Inorg. Chem.* **2015**, *54*, 3012−3021.

(40) Goodman, B. A.; Raynor, J. B. *Electron Spin Resonance of Transition Metal Complexes*; Academic Press: New York, 1970; Vol. *13*, pp 135−362.

(41) DeSimone, R. E.; Drago, R. S. *J. Am. Chem. Soc.* **1970**, *92*, 2343−2352.

(42) Patra, S.; Sarkar, B.; Mobin, S. M.; Kaim, W.; Lahiri, G. K. *Inorg. Chem.* **2003**, *42*, 6469−6473.

(43) Weisser, F.; Huebner, R.; Schweinfurth, D.; Sarkar, B. *Chem. - Eur. J.* **2011**, *17*, 5727−5736.

(44) Sarkar, B.; Schweinfurth, D.; Deibel, N.; Weisser, F. *Coord. Chem. Rev.* **2015**, *293*−*294*, 250−262.

(45) Masui, H.; Lever, A. B. P.; Auburn, P. R. *Inorg. Chem.* **1991**, *30*, 2402−2410.

(46) Lever, A. B. P. *Can. J. Chem.* **2009**, *87*, 1451−1459.

DOI: 10.1021/acs.inorgchem.5b02834
Inorg. Chem. XXXX, XXX, XXX−XXX

(47) Fulmer, G. R.; Miller, A. J. M.; Sherden, N. H.; Gottlieb, H. E.; Nudelman, A.; Stoltz, B. M.; Bercaw, J. E.; Goldberg, K. I. *Organometallics* **2010**, *29*, 2176−2179.
(48) Connelly, N. G.; Geiger, W. E. *Chem. Rev.* **1996**, *96*, 877−910.
(49) Fajer, J.; Fujita, I.; Davis, M. S.; Forman, A.; Hanson, L. K.; Smith, K. M. *Adv. Chem. Ser.* **1982**, *201*, 489−513.
(50) Tomasi, J.; Mennucci, B.; Cammi, R. *Chem. Rev.* **2005**, *105*, 2999−3093.
(51) Frisch, M. J.; et al. *Gaussian 09, Revision A.1*; Gaussian Inc.: Wallingford, CT, 2009.
(52) Roy, L. E.; Hay, P. J.; Martin, R. L. *J. Chem. Theory Comput.* **2008**, *4*, 1029−1031.
(53) Harihara, P. C.; Pople, J. A. *Theor. Chim. Acta* **1973**, *28*, 213−222.
(54) Francl, M. M.; Pietro, W. J.; Hehre, W. J.; Binkley, J. S.; Gordon, M. S.; Defrees, D. J.; Pople, J. A. *J. Chem. Phys.* **1982**, *77*, 3654−3665.
(55) Scalmani, G.; Frisch, M. J.; Mennucci, B.; Tomasi, J.; Cammi, R.; Barone, V. *J. Chem. Phys.* **2006**, *124*, 94107.
(56) Hu, K.; Severin, H. A.; Koivisto, B. D.; Robson, K. C. D.; Schott, E.; Arratia-Perez, R.; Meyer, G. J.; Berlinguette, C. P. *J. Phys. Chem. C* **2014**, *118*, 17079−17089.
(57) Sheldrick, G. M. *SHELXL Version 5*; Siemens Analytical Instruments, Inc.: Madison, WI, 1994.
(58) Sheldrick, G. M. *SADABS Version 2007/2*; Bruker AXS Inc.
(59) Sullivan, B. P.; Salmon, D. J.; Meyer, T. J. *Inorg. Chem.* **1978**, *17*, 3334−3341.
(60) Browne, W. R.; Passaniti, P.; Gandolfi, M. T.; Ballardini, R.; Henry, W.; Guckian, A.; O'Boyle, N.; McGarvey, J. J.; Vos, J. G. *Inorg. Chim. Acta* **2007**, *360*, 1183−1190.
(61) Rouffet, M.; de Oliveira, C. A. F.; Udi, Y.; Agrawal, A.; Sagi, I.; McCammon, J. A.; Cohen, S. M. *J. Am. Chem. Soc.* **2010**, *132*, 8232−8233.

DOI: 10.1021/acs.inorgchem.5b02834
Inorg. Chem. XXXX, XXX, XXX−XXX